Pore Network Modelling of Slender Packed Bed Reactors

Chemical Engineering Science 273 (2023) 118626

Contents lists available at ScienceDirect

Chemical Engineering Science

journal homepage: www.elsevier.com/locate/ces

Pore network modelling of slender packed bed reactors

A. Fathiganjehlou [1], A. Eghbalmanesh [1], M.W. Baltussen, E.A.J.F. Peters *, K.A. Buist, J.A.M. Kuipers

Multiphase Reactors Group, Department of Chemical Engineering and Chemistry, Eindhoven University of Technology, De Zaale, Eindhoven 5600 MB, the Netherlands

HIGHLIGHTS

- Slender packed beds are modeled using particle-resolved CFD.
- Pore network models (PNM) are calibrated using PR-CFD results.
- Flow profiles computed using the PNM's are in good agreement with PR-CFD results.
- Local fluctuations in the pressure field are well captured by the PNM.

ARTICLE INFO

Article history:
Received 10 January 2023
Received in revised form 2 March 2023
Accepted 6 March 2023
Available online 11 March 2023

Keywords:
Slender packed bed reactors
Pore Network Modelling
Computational Fluid Dynamics
Immersed Boundary method
Hydrodynamics

ABSTRACT

Packed bed reactors are common reactor types in chemical industries. In case of reactions with large heat effects, bundles of slender tubes are used. For such slender tubes, the column-to-particle diameter ratio, N, is small, which can give rise to significant flow channelling. This research uses two particle-scale numerical approaches, namely particle-resolved computational fluid dynamics (PR-CFD) and pore network model (PNM), to investigate the hydrodynamics of three packed beds containing random packings of spherical particles with $4.2 \leqslant N \leqslant 7.0$. Global parameters of the PNM, such as shape and constriction factors, are optimized using the PR-CFD results. A comparison of computed PNM and PR-CFD results shows that the PNM captures local variations in the bed well. The low computational cost of PNM, as well as its ability to provide locally resolved data, makes the PNM a promising approach for the pore-scale modelling of slender packed bed reactors.

1. Introduction

One of the most common reactor types applied in catalytic processes in the chemical, food, and pharmaceutical industries is the packed bed reactor. These reactors contain random packings of catalytic particles that are brought in contact with a fluid containing chemical species. The reactions performed in packed bed reactors are often either very endothermic or exothermic. In this case, in particular with flow maldistribution, cold or hot-spot can develop, respectively, with an adverse effect on reactor performance. Thus, controlling heat transport is of great importance in these reactors.

To improve the temperature control, slender reactor beds that have a low ratio of the column to particle diameter (N) are used. To further improve the heat transport in these slender packed beds, a detailed understanding of the flow dynamics is essential and will help to improve their design and performance. Because the flow dynamics largely depend on the packing configuration in slender beds, there will be a large effect of the different particle shapes and sizes. An important aspect in slender columns is the preferential flow near the column wall.

The hydrodynamics of packed bed reactors has been extensively studied both experimentally and numerically. Several experimental techniques have been used to monitor the flow inside the reactors non-invasively, e.g., particle-scale Particle Imaging Velocimetry (PIV) (Poelma, 2020) and Magnetic Resonance Imaging (MRI) (Lovreglio et al., 2018; Robbins et al., 2012). Although these experimental techniques can provide information on the local flow field, the pressure distribution cannot be readily obtained.

Numerical techniques for simulating flow in packed beds can be classified on the basis of the relevant length scale: unresolved, partially-resolved and fully-resolved particle scales. At the unresolved particle scale, 1D or 2D phenomenological models are often applied. In these models, the solid and fluid phases are modeled in an effective manner using closure relations for the hydrodynamics, mass, and heat transfer (Dixon and Partopour, 2020). These

* Corresponding author.
E-mail address: e.a.j.f.peters@tue.nl (E.A.J.F. Peters).
[1] Shared first authorship.

https://doi.org/10.1016/j.ces.2023.118626
0009-2509/

phenomenological models describe the heterogeneous nature of the particle packing by means of effective dispersion coefficients. To include radial dependence of the velocity due to the altered packing structure near a tube wall, the dispersion coefficients need a radial dependence which can be determined from experiments or particle-resolved simulations (Dudukovic, 2009; Hernandez-Aguirre et al., 2022).

In the fully-resolved particle scale (PR-CFD) approach, the governing equations are solved on a scale much smaller than the particle size. Thereby, detailed information on the spatial variation of pressure, temperature and velocity distributions can be obtained, but computationally it is very costly (Chandra et al., 2020).

The most common fully-resolved methods for packed bed reactors are the Lattice Boltzmann Method (LBM) (Zeiser et al., 2001; Zeiser, 2002) and Finite Volume Methods (FVMs) (Bai et al., 2009; Boccardo et al., 2015; Eppinger et al., 2011). The LBM method predicts the flow behavior using the Boltzmann equation using a predefined lattice. Using LBM, the Navier–Stokes equations emerge at a larger scale. However, this method often needs calibration for the "effective" particle size due to the discrete nature of the method and the treatment of the no-slip boundary at the particles (Yu and Fan, 2010). FVMs are numerical method that solves Navier–Stokes and continuity equations where the no-slip boundary at the particles is applied via different techniques (Jurtz et al., 2019; Dixon et al., 2013; Finn and Apte, 2013; Wongkham et al., 2020). One of these techniques is the boundary-fitted method, where the computational mesh for solving the governing equations conforms to the shape of the solid boundaries defined by the particles. The main challenge of this method is the creation of the mesh at the contact points of the solid phases (i.e. the particle–particle and the particle–wall contact points) (Dixon et al., 2013).

In this study, the Immersed Boundary Method (IBM) has been adopted which uses an uniform Cartesian computational grid. The no-slip boundary condition at the fluid–solid interface is enforced via an implicit second order technique (Deen et al., 2012).

The partially-resolved models bridge the gap between the unresolved and fully-resolved scales. In comparison to unresolved models, the partially-resolved models provide more detailed results at the local level, while partially resolved models require less computational resources compared to fully-resolved models. In this paper, we will consider Pore Network Model (PNM), as the partially-resolved method. PNM uses the 3D structural information of a porous medium and converts it into a simplified network of pore bodies and throats. Because PNM is obtained from the structural information of the porous medium, the structural information is embedded inside the pore network model, which is another advantage of PNM to the unresolved models that only apply these effects by effective coefficients (Hernandez-Aguirre et al., 2022).

The PNM method has been used for various applications, particularly in the fields of petroleum and geoscience engineering (Xiong et al., 2016; Morimoto et al., 2022; Sufian et al., 2019). In addition, Larachi et al. (2014) investigated the application of PNM for determination of the packed beds' pressure drop. Liu et al. (2020) also employed PNM to investigate the flow through a packed bed filled with various shapes and sizes of packings, e.g. spheres, cylinders, Raschig rings and trilobes. Hannaoui et al. (2015) have used the PNM to model the two-phase gas–liquid flow in a trickle bed reactor and were able to predict the pressure drop and saturation values at different gas and liquid flow rates.

In the analysis of the hydrodynamics using PNM, the flow resistance through the pore network model is attributed to the throats. The simplest model for a throat is that of a cylinder with a constant circular cross-section. Because this is not a valid approximation, various methods have been investigated to improve it, e.g. calibrating the PNM with experiments (Larachi et al., 2014), empirical correlations (Hannaoui et al., 2015) or particle-resolved numerical methods (Rabbani and Babaei, 2019; Raeini et al., 2017) and improving the approximation using the geometrical information of the packed bed (Øren and Bakke, 2003; Mason and Morrow, 1991). The friction loss can for example be tuned by defining an effective radius, r_{ij}^{e}, for each throat by multiplying each throat radius by a global correction factor named the throat effective aspect ratio (Larachi et al., 2014). This aspect ratio is determined by fitting the PNM pressure losses to the known bed pressure loss in the Darcy regime (Larachi et al., 2014; Hannaoui et al., 2015).

Raeini et al. (2017) used a single-phase PR-CFD to determine the resistance inside individual throats. After extracting the PNM, each pore is subdivided into sub-elements called half-throat connections, which are subdivided into corners. The resistance of each corner is determined separately to ensure that the extracted pore network can represent the flow permeability exactly. Finally, Rabbani and Babaei (2019) combined LBM with a machine learning approach to correct the throat resistances. They trained a neural network for throat permeability on basis of the throat cross-sectional images created from LBM simulations.

Previous studies on hydrodynamics in packed columns using PNM typically extract the PNM for a representative volume element, usually a uniform cubical domain of the column. This will not provide the understanding of the flow behavior in the entire packed bed due to the channelling near the column wall. To include these effects, we extract the PNM from the entire packed bed. This approach enables the characterization of flow maldistribution and pore-level pressure fluctuations.

As the pores and throats are discrete entities, it is difficult to obtain a smooth flow and velocity profile. To address this issue, we introduce a novel post-processing step in this study, which divides the throats in the PNM in thousands of sub-throats. In each throat, a laminar velocity profile is assumed. This approach enables us to obtain local velocity and flow profiles which were not reported for PNM before.

In this paper, the applicability of PNM for slender packed beds, especially the preferential flow, is investigated. To enable this investigation 3D structures of a cylindrical packed column of 3, 4 and 5 mm diameter spherical particles are generated using the rigid body technique of Blender (Bender et al., 2014). The generated packed beds have a range of $4.2 \leqslant N \leq 7.0$.

The pore network models based on the created 3D structure of the column are calibrated with PR-CFD on basis of the pressure drop over the packed beds at different Reynolds numbers. The parameters for this calibration are the throat radius scaling factor, $\mathscr{F}$, the expansion curvature factor, m, and the contraction curvature factor, n (Larachi et al., 2014). The calibrated PNM is used to investigate the preferential flows inside the packed beds by the average flow fields, radial velocity and flow profiles. Furthermore, the pressure field is compared to determine if the heterogeneities in the pressure fields at the pore level are captured.

In the following sections, the method used for generating the random packings for the simulations is discussed first. Then, the PR-CFD and the PNM are explained. In the results and discussion section, the results of the PR-CFD and the PNM are compared in terms of the fluid velocity and pressure fields.

2. Methods

2.1. Packing generation

The first step for the investigation of packed bed reactors is the generation of the particle packings. In this work, three packings are generated with particle diameters equal to 3, 4 and 5 mm. These packings are generated using Blender (Blender Online Community, 2018), which uses the Rigid-Body Dynamics (RBD)

approach for packing generation. The collisions of particles are calculated on basis of the primitive shape of the particles where the surface of the particles will not deform during the collision. In addition, the particles collision are assumed to be inelastic (Blender Online Community, 2018; Flaischlen and Wehinger, 2019). Flaischlen and Wehinger (2019) validate the RBD approach with an experiment by Giese et al. (1998). To pack the particles in the column, all the particles are poured into the column using a cone at the top of the column. Table 1 shows the physical properties for the generation of the particle packing. These packings are used in both PR-CFD and PNM simulation.

2.2. Computational fluid dynamics

The PR-CFD model solves the Navier–Stokes and continuity equations assuming an incompressible and Newtonian fluid with constant material properties (Eqns. (1) and (2), respectively).

$$\rho\frac{\partial \mathbf{u}}{\partial t} = -\nabla p - \rho\nabla\cdot\mathbf{uu} - \nabla\cdot\boldsymbol{\tau} + \rho\mathbf{g} \tag{1}$$

$$\nabla\cdot\mathbf{u} = 0 \tag{2}$$

These equations are solved on a staggered grid. The time integration is performed using a first order backward Euler method. The convective fluxes are discretized using a second order Barton scheme, which is treated semi-implicitly using deferred correction. The stress tensor is discretized using a second central differencing scheme and solved semi-implicitly. The implicit terms in the stress tensor are chosen such that the different velocity components can be solved separately while the derivatives involving other velocity components are treated explicitly. To solve Eqns. (1) and (2) a projection-correction algorithm is used which predicts the velocity field from the Navier–Stokes equations and corrects it to comply with the continuity equation. The implicit parts of the Navier–Stokes equations are solved using an in–house BiCGSTAB-2 solver with incomplete LU decomposition preconditioner from open source Trilinos 12.18.1. The correction step is also solved using the BiCGSTAB-2 solver but with using Algebraic Multigrid (AMG) preconditioner of Trilinos 12.18.1.

The 3D spatial discretization leads to 7-point stencil in space. If one of the neighboring cells is located inside a solid phase, the no-slip boundary condition at the particle is applied using a second-order directional extrapolation of the velocity on the fluid cells and the value at the boundary of the solid object. When the solid surface is close to the fluid cell (in this work, 0.05 times the grid spacing), the extrapolation is changed from second order to first order. In addition, the extrapolation will be adjusted to include both no-slip boundaries when two particles are close, i.e. within 2 grid cells. A more detailed explanation of this method can be found in the work by Deen et al. (2012).

Table 1
The geometrical parameters of the packing of spherical particles.

	Value	Unit
Particle diameter (d_p)	0.003, 0.004, 0.005	m
Column diameter (D)	0.021	m
Column to particle diameter ratio (N)	7, 5.25, 4.2	-
Number of particles	725, 325, 160	-
Restitution coefficient	0.0	-
Friction coefficient	0.5	-
Length of the bed	0.056, 0.061, 0.059	m

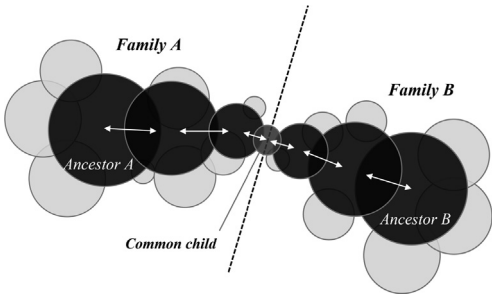

Fig. 1. Maximal ball family clusters. The largest maximal ball in each family cluster is named the ancestor and the common child of the two families represents a throat that connects two families. The black balls are on the pore-throat chain, which is shown by white arrows. The gray balls are pore bodies that are not on the pore-throat chain, but they attribute to the pore volume. (adjusted from Dong and Blunt (2009)).

2.3. Pore network modelling

The PNM is created from the 3D image of the packed bed. The acquired 3D volume of the packed bed is voxelized using cubical volume units, segmented, and binarized. The pore network can be extracted from the binarized 3D volume image using several methods, e.g. the maximal ball (Liu et al., 2020; Silin and Patzek, 2006; Dong and Blunt, 2009) and medial axis methods (Larachi et al., 2014; Al-Raoush and Willson, 2005; Al-Raoush et al., 2003; Lindquist et al., 1996). According to the literature, the maximal ball method is preferred as the definition of the pores, throats, and the

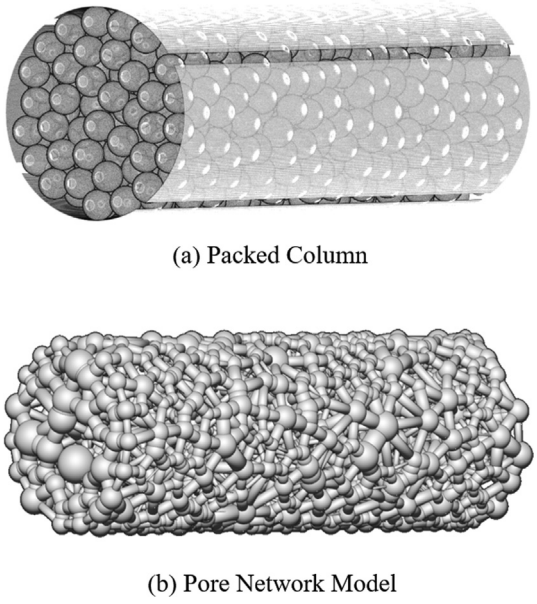

Fig. 2. A schematic of (a) a packed column and (b) the extracted pore network model.

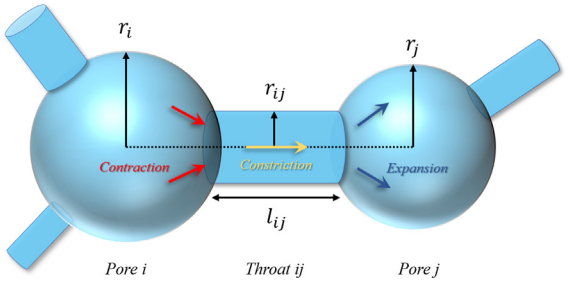

Fig. 3. A schematic of a pore-throat-pore element in a pore network model.

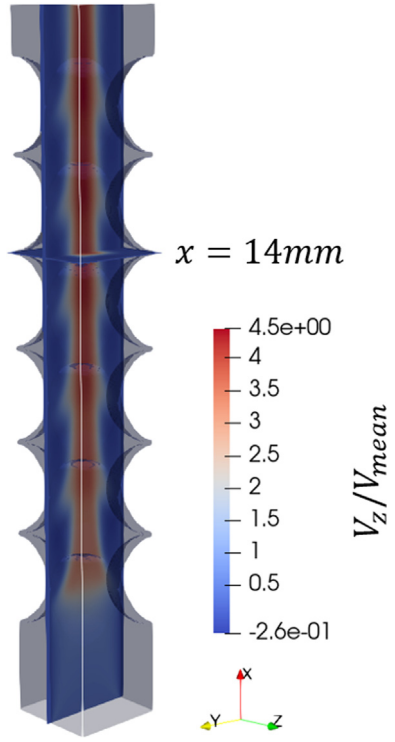

Fig. 4. The velocity contours from PR-CFD simulation in the structured packed beds of spheres (Suekane et al., 2003) and position of the mid plane for the results in Fig. 5.

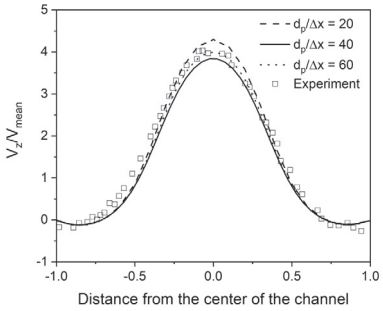

(a) $Re_{pore} = 59.78$

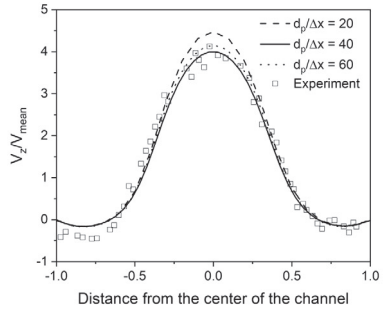

(b) $Re_{pore} = 105.57$

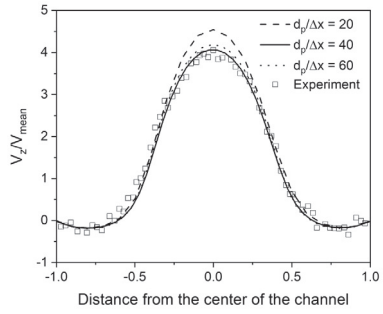

(c) $Re_{pore} = 204.74$

Fig. 5. A comparison of the normalized velocity over the normalized distance from the center of the channel at the plane indicated in Fig. 4. Each graph shows a set of different resolutions, expressed as number of grid-cells per sphere diameter.

connectivity of the network is closer to reality (Jiang et al., 2007). Therefore, the pore network in this research will be extracted based on the maximal ball extraction method of Raeini et al. (2017), which is a generalized version of the method developed by Dong and Blunt (2009).

In the maximal ball method, a sphere is generated and expanded at each void voxel until it touches the surface of a particle or the column wall. The spheres located entirely inside other spheres are eliminated. The remaining spheres, called the maximal balls, are clustered into cluster families to define the pore-throat chains (Fig. 1). After clustering, the locally largest maximal ball is considered a pore body, and the overlapping neighboring maximal balls are absorbed into the pore bodies volume. A common child of two clusters represents a throat that serves as a connection between two pore bodies. The important characteristics of the pore network model (e.g. the pore and throat radius, throat length and connectivities), are determined from the topological information. Fig. 2 shows a visualization of a packed bed and the corresponding pore network model.

In order to enable the quantitative analysis of flow phenomena in the extracted model, the mechanical energy balance and mass balance are solved for each pore-throat-pore element, which is schematically shown in Fig. 3. When the fluid flows from pore i to throat ij, there is a pressure loss due to the contraction. Similarly, there is a pressure loss due to the sudden expansion of the flow cross-section when the fluid enters pore j from throat ij. Finally, pressure loss in the throat ij is estimated by assuming Hagen-Poiseuille flow in the throat. By combining the mechanical energy balances and the pressure losses, the overall pressure drop along the pore-throat-pore element is (Liu et al. (2020)):

$$P_i - P_j = A_{ij} l_{ij} + C_{ij} + E_{ij} - \frac{\gamma}{2\pi^2}\rho q_{ij}^2\left(\frac{1}{r_i^4} - \frac{1}{r_j^4}\right) \tag{3}$$

In Eq. (3), P_i and P_j are the pressure values in pores i and j, respectively, and q_{ij} is the volumetric flow rate in throat ij. γ is the flow pattern constant, which is set to 1 as an initially flat velocity profile is assumed. A_{ij}, C_{ij} and E_{ij} are the constriction, contraction, and expansion dissipation loss factors, respectively, and are defined as:

$$A_{ij} = \frac{8\mu_f q_{ij}}{\pi r_{ij}^4} \tag{4}$$

$$E_{ij} = \frac{\rho_f}{2\pi^2}\frac{q_{ij}^2}{r_{ij}^4} \times \left[\left(\frac{E_0}{Re_{ij}}\right)^m + \left(1 - \frac{r_{ij}^2}{r_j^2}\right)^{2m}\right] \tag{5}$$

$$C_{ij} = \frac{\rho_f}{2\pi^2}\frac{q_{ij}^2}{r_{ij}^4} \times \left[\left(\frac{C_0}{Re_{ij}}\right)^n + \frac{1}{2^n}\left(1 - \frac{r_{ij}^2}{r_i^2}\right)^n\right] \tag{6}$$

In these equations, Re_{ij} is the Reynolds number in throat ij, and C_0 and E_0 are the laminar constants for contraction and expansion,

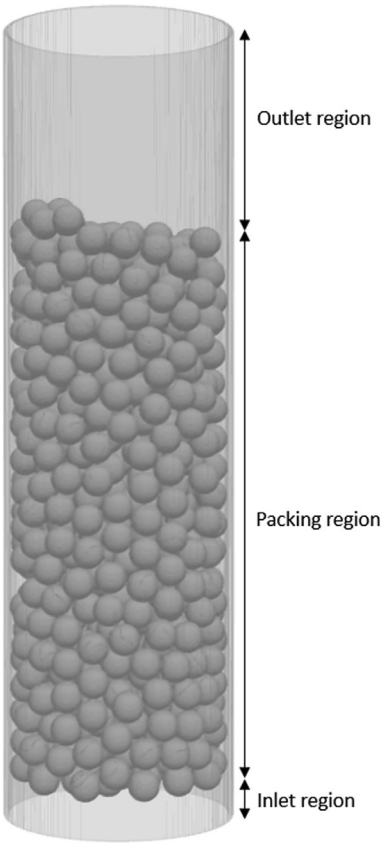

Fig. 6. Schematic graph for the spherical packed bed with the $d_p = 3$mm which is used for the PR-CFD simulations.

which are equal to 26 and 27, respectively, for a broad range of Re_{ij} (Larachi et al., 2014). n and m are the contraction and expansion curvature factors, which will serve as calibration parameters of the pore network model.

In order to find the pressure and the flow rate in each pore and throat, the mass balance equation is based on Kirchhoff's current law.

$$\sum_{j=1}^{z} q_{ij} = 0 \tag{7}$$

In Eq. (7), z is the connectivity, i.e. the number of pores pore i is connected to. There is a mass balance equation for each pore, and a total pressure drop equation for each throat. The nonlinear system of equations is solved by defining an incidence matrix (***inc***) representing the connection between the pores and throats, i.e. in ***inc***, -1 is set for pore i and $+1$ for pore j to represent flow from pore i to pore j. The mass balance equation can as a result be written in matrix form given by Eq. (8) using the incidence matrix.

$$\boldsymbol{inc} \times \vec{q} = 0 \tag{8}$$

Where $\vec{q}$ is the flow rate vector of the throats. Combining Eqs. (3) to (6), the pressure drop inside the PNM can be obtained by solving Eq. (9).

$$\vec{q} = \boldsymbol{\alpha} \times \vec{P} \tag{9}$$

Where $\vec{P}$ is the pressure field in the pore bodies of the PNM, and $\boldsymbol{\alpha}$ is the factor matrix of which each element is defined as Eq. (10). This system of equations can be solved iteratively by a direct substitution approach.

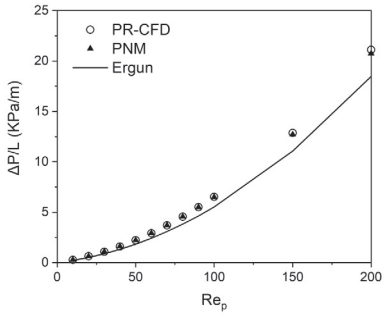

(a) $d_p = 3$ mm

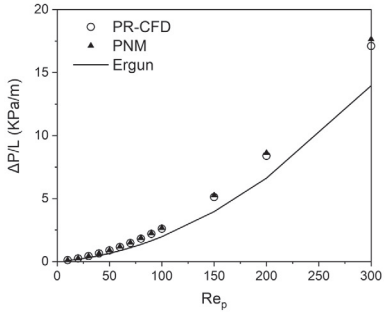

(b) $d_p = 4$ mm

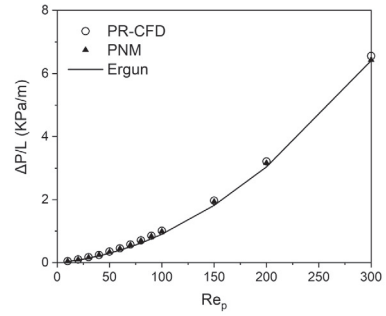

(c) $d_p = 5$ mm

Fig. 7. Pressure drop over the packed beds at various particle Re numbers (Re_p). The relative root mean squared of the difference between PNM and PR-CFD pressure drops is 0.87%, 2.12% and 3.11% for packed beds of 3, 4 and 5 mm spherical particles, respectively.

$$\alpha_{ij} = \left(\frac{\pi r_{ij}^4}{8\mu_f l_{ij}}\right) + \frac{2\pi^2}{\rho_f}\frac{r_{ij}^4}{|q_{ij}|} \times \left[\left(\frac{C_0}{Re_{ij}}\right)^n + \frac{1}{2^n}\left(1 - \frac{r_{ij}^2}{r_i^2}\right)^n\right]^{-1} + \frac{2\pi^2}{\rho_f}\frac{r_{ij}}{|q_{ij}|} \times \left[\left(\frac{E_0}{Re_{ij}}\right)^m + \left(1 - \frac{r_{ij}^2}{r_j^2}\right)^{2m}\right]^{-1} - \frac{2\pi^2}{\gamma} \times \frac{1}{\rho|q_{ij}|}\left[\left(\frac{1}{r_i^4} - \frac{1}{r_j^4}\right)\right]^{-1} \tag{10}$$

The inlet and outlet boundary conditions are introduced by extra inlet and outlet throats which are connected to the inlet and outlet pores based on the geometrical information. The flow to the column is distributed over the inlet throats based on the area of the throat, i.e. a throat with a large area will obtain a correspondingly larger part of the flow. At the outlet throats, the absolute pressure is set to the atmospheric pressure.

Although PNM assumes a throat to have a cylindrical shape with a specific length and radius, the real throats have more

complex and irregular shapes which depend on the particle packing. To correct for this simplification, the following scaling factor ($\mathscr{F}$) is used in this work.

$$\mathscr{F} = \frac{r_{ij}^{eff}}{r_{ij}} \tag{11}$$

In Eq. (11), r_{ij} is the radius of the simplified representation of throat ij, and r_{ij}^{eff} is the effective throat radius. In this study, the overall pressure drop over the bed obtained in the PR-CFD simulations is used to determine the optimal values for the fitting parameters. Next to $\mathscr{F}$, the fitting parameters are m and n of Eqns. (5) and (6), respectively. These optimized parameters are used to determine the flow rates in the throats and obtain the flow and pressure profiles, which are compared to the PR-CFD results.

3. Results and discussion

In this section, the validation of the PR-CFD method and the calibration of the PNM with CFD will be discussed. Furthermore, the pressure and flow fields from PNM will be compared to the PR-CFD simulation results.

3.1. Validation of the Particle-resolved CFD Method

The implemented PR-CFD model in a dense particle system is verified previously by Deen et al. (2012). In addition, the method is validated in this work by a comparison with the experimental work of Suekane et al. (2003) using Magnetic Resonance Imaging. The flow inside a structured packed bed of spheres, which is shown in Fig. 4 is simulated for validating the velocity profiles in PR-CFD method. The bed consists of six touching layers of four spheres with centers located at the edges of the channel. The simulations were performed in the laminar flow regime with pore Reynolds numbers, $59.78 < Re_{pore} = \rho V_{mean} D_p/\mu = \rho V_{inlet} D_p/\varepsilon\mu < 205$, where ε is the average bed porosity.

Fig. 5 shows the comparison of the normalized velocity profile of the fluid between the fourth and fifth layers of spheres at the mid-plane for different Re_{pore} of the experimental results (Suekane et al., 2003) and our simulation results at different resolutions ($d_p/\Delta x$ = 20, 40, and 60). This figure shows that our simulation results agree well with the experimental results. The normalized root-mean-square deviation of the simulation with resolution 40 grids per diameter of the particle compared to the finest mesh is 0.02. As this deviation is well below the experimental accuracy of the experiments, a resolution of 40 $d_p/\Delta x$ is used in the remainder of the paper.

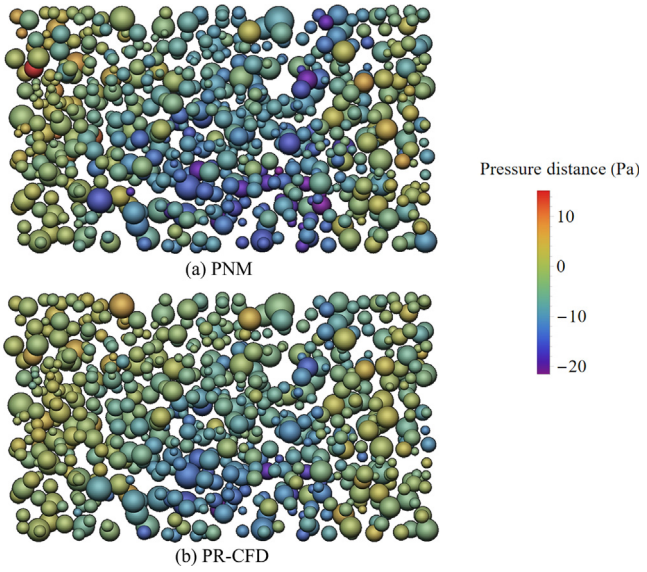

Fig. 8. The pore pressure with respect to the macroscopic pressure for the packed bed of 3mm particles at $Re_p = 100$.

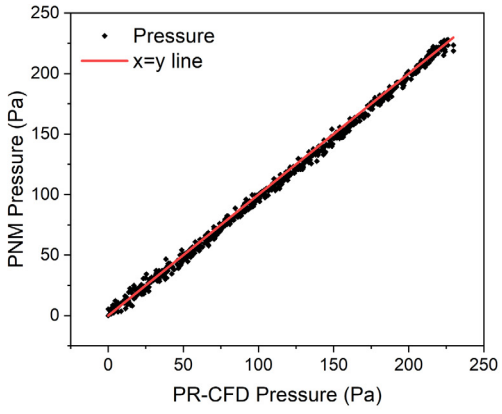

(a) $d_p = 3$ mm

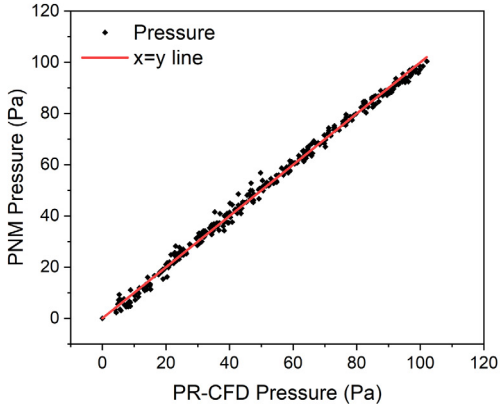

(b) $d_p = 4$ mm

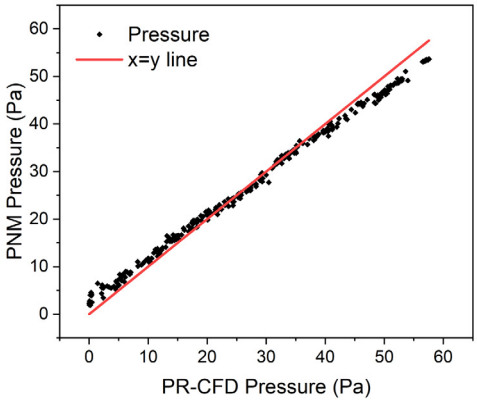

(c) $d_p = 5$ mm

Fig. 9. The parity plots of the pressure field from PNM and from PR-CFD at $Re_p = 100$. In this parity plot, only the measurement section is included.

3.2. Flow inside a packed bed of spheres

3.2.1. Simulation settings

Using the particle packings created with Blender, the simulations were performed for different particle Reynolds numbers (Re_p = 10, 20, 30, 40, 50, 60, 70, 80, 90, 100, 150, 200, 300). For all the simulations water is used as the fluid phase. To exclude inlet and outlet effects, only a section of the packing is used in the post processing of the results, i.e. the first 0.008 m and the last 0.012 m from the bed are not considered in the post processing.

Fig. 6 shows the packing as used in the PR-CFD simulations. This figure shows that an inlet region of 0.004 m and an outlet region are added to the bed. The length of the outlet region for the simulations with $Re_p < 50$ is 15, 8 and 10 mm for the packing of 3, 4 and 5 mm particles, respectively. For the simulations with $Re_p > 50$ the outlet region equals to 40mm for the 3 mm particles and equals to 20mm for the packing of 4 and 5 mm particles. Finally, the viscosity of the liquid is gradually increased by a factor 100 starting from 0.015m from the outlet boundary to avoid recirculation over the outflow boundary. For the PR-CFD simulations, the pressure at the outlet is prescribed.

3.2.2. Calibration of the pore network model

To calibrate the PNM, the network is fitted on basis of the overall pressure drop for all Re_p and N using a multi-variable search approach, the Genetic Algorithm (GA) of the optimization toolbox v8.3 of Matlab 2019a (The MathWorks, 2019). The variables changed for the optimization are the scaling factor ($\mathscr{F}$), the expansion curvature factor (m) and the contraction curvature factor (n). With a relative root mean squared error of 2.04%, the optimal parameters are:

$\mathscr{F}^{opt} = 1.477$
$m^{opt} = 1.507$
$n^{opt} = 0.296$

Fig. 7 shows a good comparison of the pressure drop obtained using PNM, PR-CFD and the Ergun correlation (Ergun, 1952).

3.2.3. Pressure profile

Using the calibrated parameters, the local pressure fields are compared for both PNM and PR-CFD to determine the capability of PNM to capture the local heterogeneities in the pressure field. In this comparison, the calculated pressures in the pores of the PNM are considered, while the pressure of the PR-CFD is deter-

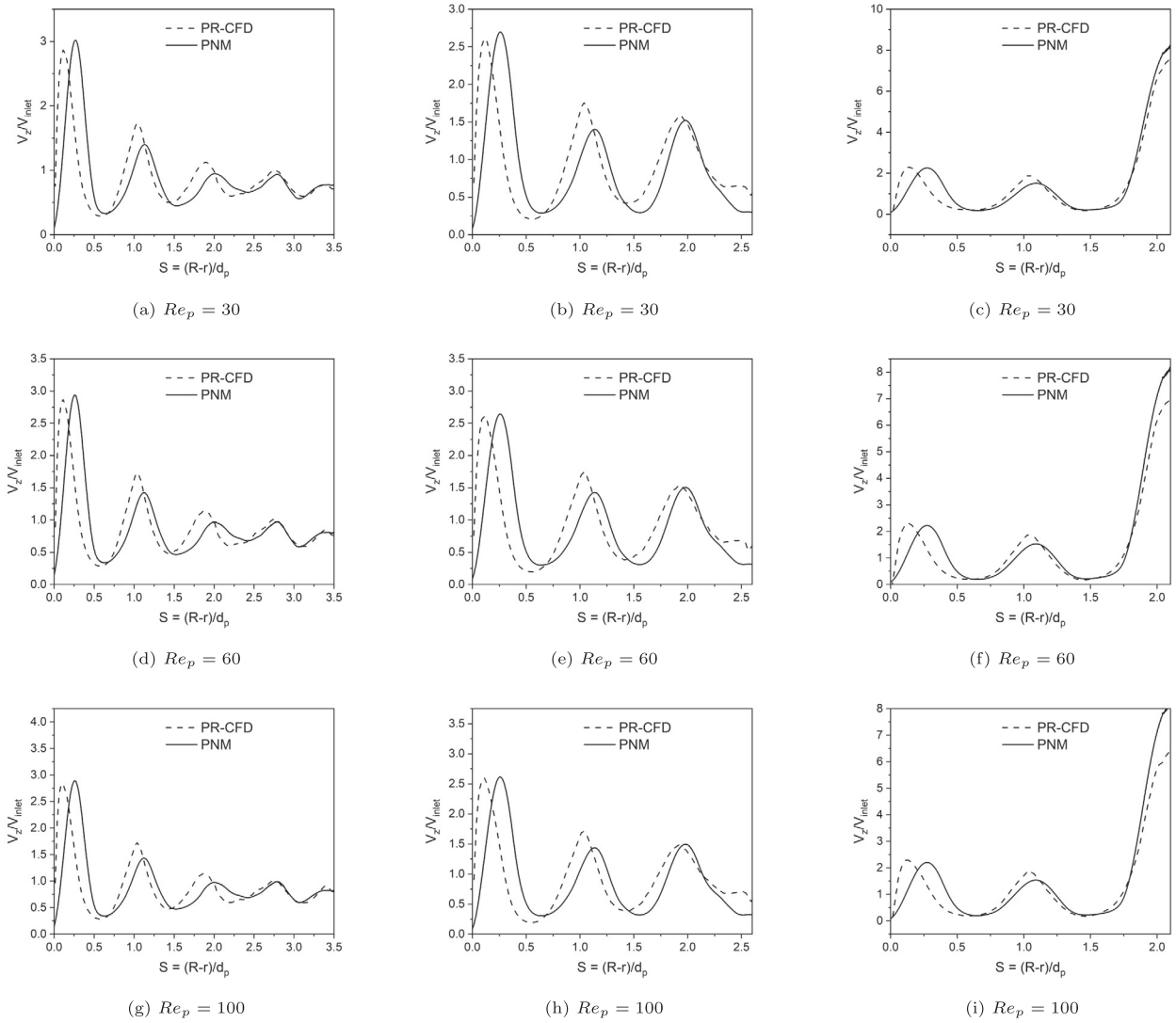

(a) $Re_p = 30$ (b) $Re_p = 30$ (c) $Re_p = 30$

(d) $Re_p = 60$ (e) $Re_p = 60$ (f) $Re_p = 60$

(g) $Re_p = 100$ (h) $Re_p = 100$ (i) $Re_p = 100$

Fig. 10. Radial profiles of the averaged dimensionless superficial velocity for a,d,g) $N = 7$, b,e,h) $N = 5.25$, and c,f,i) $N = 4.2$ spherical packings for PR-CFD and PNM simulations versus the dimensionless distance from the wall (S).

mined by averaging all pressures of a virtual pore with the center and size of the PNM. A schematic representation of this one-to-one comparison is shown in Fig. 8.

Fig. 9 shows the parity plots of this pore-level pressure in PNM and in PR-CFD at $Re_p = 100$. This figure shows that there is a good match between the pore-level pressure values from PNM and PR-CFD for 3 and 4 mm particles. However, this correspondence is less satisfactory for 5 mm particles, which could be caused by the lower resolution in the PNM as the number of pore-throat-pore elements decreases with an increasing particle size.

In addition, the PNM also has a larger deviation for the overall pressure drop for the 5 mm particles, which might also explain part of differences. To determine the possibility to capture the local pressure variations, the magnitude of local pressure fluctuations are compared using a coefficient of determination, R^2:

$$R^2 = 1 - \frac{\sum_i (p_{i,PR-CFD} - p_{i,PNM})^2}{\sum_i (p_{i,PR-CFD} - p_{macro}(z_i))^2}, \tag{12}$$

where $p_{macro}(z_i)$ is the axial pressure profile that is obtained from the PR-CFD by cross-sectional averaging. If R^2 is significantly larger than 0, a large part of the local pressure variations is captured by the PNM.

For the packed beds of 3, 4 and 5 mm particles, R^2 is $0.65, 0.62$ and -0.59, respectively. This implies a good match in the heterogeneities of the pressure for the packed column of 3 and 4 mm particles, while the negative R^2 for the 5 mm particles points to either no correlation in the local pressure profile or a difference in the overall pressure drop in the PNM and PR-CFD. In this case, Fig. 9 (c) indicates that the overall pressure drop does not match. Therefore, the local pressure profiles are also compared to the PNM calibrated with only packed beds of a single particle size, i.e. the PNM is created separately for 3, 4 and 5 mm particles. In this approach, R^2 is $0.72, 0.62$ and 0.56 respectively, which shows that the low R^2 values are due to the difference in the overall pressure drop.

3.2.4. Flow field

To investigate the predictive capabilities of the PNM for the flow structures in slender packed beds, the flow fields, the radial velocity profiles and flow rates of the calibrated PNM are compared to the results from PR-CFD. Fig. 10 shows the radial profiles of the averaged dimensionless superficial velocity. As the pores and throats are discrete entities, the radial profile in the pore network

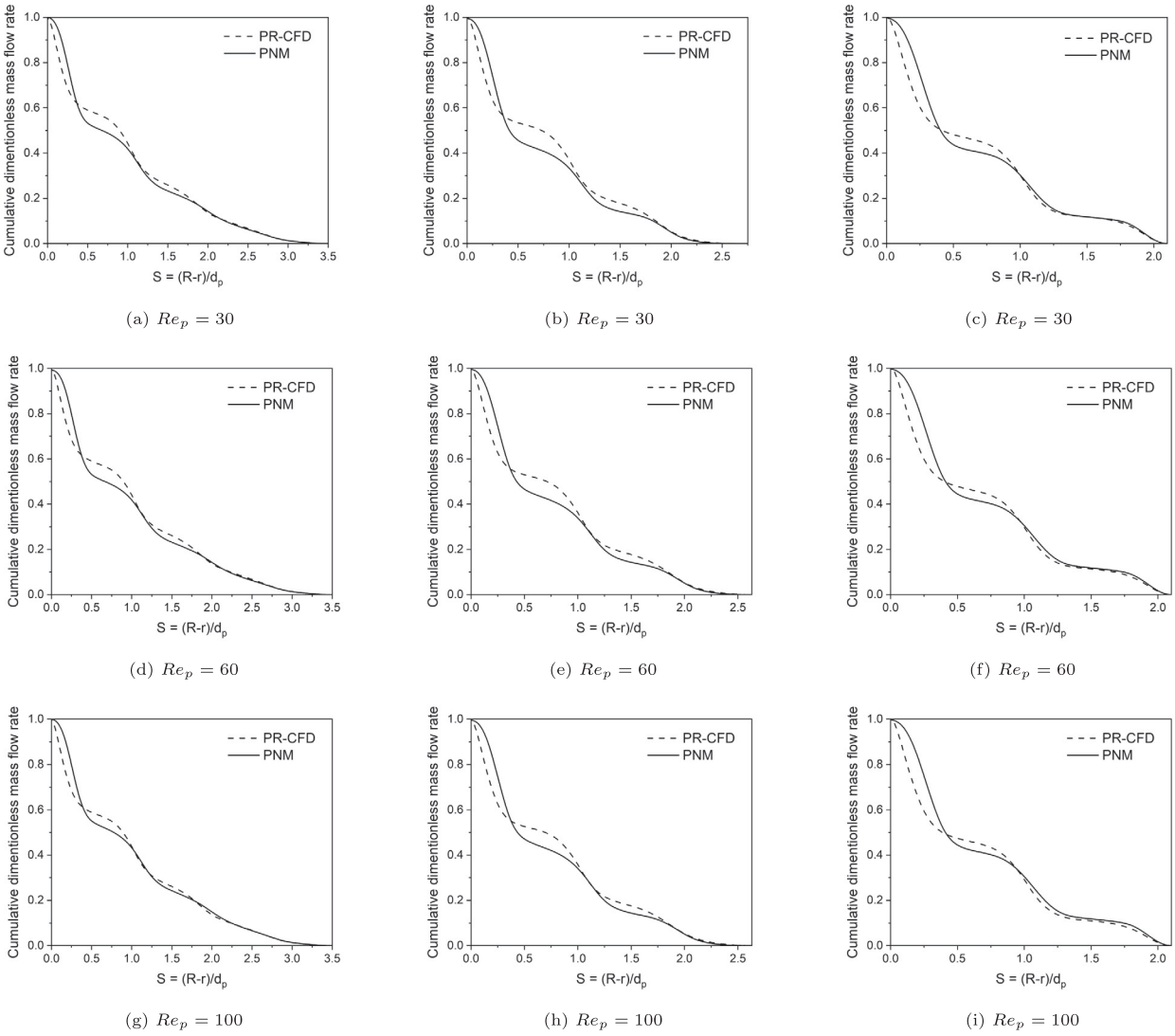

Fig. 11. Radial profiles of dimensionless cumulative flow rate profile for $N = 7$ (a,d,g), $N = 5.25$ (b,e,h), and $N = 4.2$ (c,f,i) spherical packings for PR-CFD and PNM simulations versus the dimensionless distance from the wall (S).

model is created by subdivision of the throats in 2500 subthroats in angular direction and 50 subthroats in radial direction. The velocity profile assigned to each subthroat is based on a parabolic velocity profile inside the throat. The flow rate of each subthroat corresponds to this velocity profile integrated over the area associated with it.

Fig. 10 shows that the PNM is able to capture the flow field in all three packed beds, as the trends and the number of peaks of the radial velocity profiles are similar. However, there are some differences, e.g. the shift of the peaks particularly in the areas close to column wall. These differences are probably caused by the discrete nature of the PNM.

In addition, the cylindrical throats are representing flow channels with arbitrary shapes. The effect of this difference in throats shape will shift and/or broaden the peaks. However, it is expected that on length scales larger than a pore diameter, the flow rates will correspond. In order to investigate this, the radial cumulative flow rates are plotted in Fig. 11. The jumps in these flow profiles show the preferential flows. The significant jump in the region close to the column wall ($S \leq 0.5$) indicates intense channeling near the column wall. Around 40 to 60 percent of the flow passes through this region. This amount increases with decreasing the column to particle aspect ratio, i.e. in more slender packed beds.

4. Conclusion and outlook

In this research, the effectiveness of simulating slender packed beds with PNM was investigated for randomly packed beds of spherical particles with three different column-to-particle aspect ratios (N = 7, 5.25 and 4.2). Based on the pressure drop for particle Reynolds numbers of $10 - 200$, the PNM was fitted using the fitting coefficient ($\mathscr{F}$), the expansion factor (m) and the contraction factor (n). Using a global optimization, the optimal values of $m = 1.507, n = 0.296$, and $\mathscr{F} = 1.477$ were obtained. Only for the largest particle size, i.e. smallest N, there is a systematic deviation of the overall pressure drop. Using the optimal parameter values in PNM, the pressure profile at the pore level was compared. The local pressure variations inside pores are well predicted except for the bed with $N = 4.2$. However, when the PNM parameters were fitted only on this bed, a good correspondence could also be obtained for the local pressure variations.

To compare the radial velocity profiles, the throats of the PNM were subdivided in 50 radial and 2500 angular subthroats, which are assigned a flow rate based on a parabolic velocity profile in the throat. Both PR-CFD and the PNM show channeling along the wall. There are some differences in the radial flow and velocity profiles from PNM compared to PR-CFD, which are related to the discrete nature of the PNM. Although it was partly corrected by subdividing throats, some disagreement remains, which is probably due to the irregular shape of the real throats.

As the PNM requires far less computational time compared to the PR-CFD method, PNM is a promising technique for fast determination of the flow inside a slender packed bed. It would be interesting to determine the possibilities in PNM to model other transport phenomena, such as solute dispersion, reaction systems, and heat and mass transfer. Furthermore, PNM is more suitable for modeling large-scale industrial packed bed reactors where PR-CFD techniques may not be computationally feasible. As the non-uniform flow distribution is captured by the PNM, there is a good possibility that other heterogeneities can also be represented by PNM. In addition, there are some differences between the radial profiles from PNM and PR-CFD, especially close to the column wall. These differences might be decreased even further by a geometrically more sophisticated representation of pores and throats, as well as their subdivision near the column wall.

In addition, future studies could investigate the capabilities of PNM at higher Reynolds numbers and compare its results with PR-CFD simulations or experiments, as this would be closer to industrial-scale packed bed reactors.

Data availability

Data will be made available on request.

Declaration of Competing Interest

The authors declare that they have no known competing financial interests or personal relationships that could have appeared to influence the work reported in this paper.

Acknowledgement

This work is a part of the research program TOP Grants Chemical Sciences with project number 716.018.001, which is financed by the Dutch Research Council (NWO). The authors also thank Noah Romijn for her kind help in generating the particle packings in the Blender software. In addition, we thank SURF (www.surf.nl) for the support in using the National Supercomputer Snellius.

References

Al-Raoush, R.I., Willson, C.S., 2005. Extraction of physically realistic pore network properties from three-dimensional synchrotron X-ray microtomography images of unconsolidated porous media systems. J. Hydrol. 300 (1–4), 44–64.
Al-Raoush, R., Thompson, K., Willson, C.S., 2003. Comparison of network generation techniques for unconsolidated porous media. Soil Sci. Soc. Am. J. 67 (6), 1687–1700.
Bai, H., Theuerkauf, J., Gillis, P.A., Witt, P.M., 2009. A coupled dem and cfd simulation of flow field and pressure drop in fixed bed reactor with randomly packed catalyst particles. Industr. Eng. Chem. Res. 48 (8), 4060–4074.
Bender, J., Erleben, K., Trinkle, J., 2014. Interactive simulation of rigid body dynamics in computer graphics. Comput. Graph. Forum 33 (1), 246–270.
Boccardo, G., Augier, F., Haroun, Y., Ferré, D., Marchisio, D.L., 2015. Validation of a novel open-source work-flow for the simulation of packed-bed reactors. Chem. Eng. J. 279, 809–820.
Chandra, V., Peters, E.A.J.F., Kuipers, J.A.M., 2020. Direct numerical simulation of a non-isothermal non-adiabatic packed bed reactor. Chem. Eng. J. 385, 123641.
B.O. Community, 2018. Blender - a 3d modelling and rendering package, http://www.blender.org.
Deen, N.G., Kriebitzsch, S.H.L., van der Hoef, M.A., Kuipers, J.A.M., 2012. Direct numerical simulation of flow and heat transfer in dense fluid–particle systems. Chem. Eng. Sci. 81, 329–344.
Dixon, A.G., Partopour, B., 2020. Computational fluid dynamics for fixed bed reactor design. Annu. Rev. Chem. Biomol. Eng. 11, 109–130.
Dixon, A.G., Nijemeisland, M., Stitt, E.H., 2013. Systematic mesh development for 3D CFD simulation of fixed beds: contact points study. Comput. Chem. Eng. 48, 135–153.
Dong, H., Blunt, M.J., 2009. Pore-network extraction from micro-computerized-tomography images. Physical review E 80 (3), 036307.
Dudukovic, M.P., 2009. Frontiers in reactor engineering. Science 325 (5941), 698–701.
Eppinger, T., Seidler, K., Kraume, M., 2011. DEM-CFD simulations of fixed bed reactors with small tube to particle diameter ratios. Chem. Eng. J. 166 (1), 324–331.
Ergun, S., 1952. Fluid flow through packed columns. Chem. Eng. Prog. 48, 89–94.
Finn, J., Apte, S.V., 2013. Relative performance of body fitted and fictitious domain simulations of flow through fixed packed beds of spheres. Int. J. Multiphase Flow 56, 54–71.
Flaischlen, S., Wehinger, G.D., 2019. Synthetic packed-bed generation for CFD simulations: Blender vs. STAR-CCM+, ChemEngineering 3 (2), 52.
Giese, M., Rottschafer, K., Vortmeyer, D., 1998. Measured and modeled superficial flow profiles in packed beds with liquid flow. Am. Insti. Chem. Eng. AIChE J. 44 (2), 484.
Hannaoui, R., Horgue, P., Larachi, F., Haroun, Y., Augier, F., Quintard, M., Prat, M., 2015. Pore-network modeling of trickle bed reactors: Pressure drop analysis. Chem. Eng. J. 262, 334–343.
Hernandez-Aguirre, A., Hernandez-Martinez, E., Lopez-Isunza, F., Castillo, C.O., 2022. Framing a novel approach for pseudo continuous modeling using direct numerical simulations (DNS): Fluid dynamics in a packed bed reactor. Chem. Eng. J. 429, 132061.

Jiang, Z., Wu, K., Couples, G., Van Dijke, M.I.J., Sorbie, K.S., Ma, J., 2007. Efficient extraction of networks from three-dimensional porous media. Water Resour. Res. 43 (12).
Jurtz, N., Kraume, M., Wehinger, G.D., 2019. Advances in fixed-bed reactor modeling using particle-resolved computational fluid dynamics (CFD). Rev. Chem. Eng. 35 (2), 139–190.
Larachi, F., Hannaoui, R., Horgue, P., Augier, F., Haroun, Y., Youssef, S., Rosenberg, E., Prat, M., Quintard, M., 2014. X-ray micro-tomography and pore network modeling of single-phase fixed-bed reactors. Chem. Eng. J. 240, 290–306.
Lindquist, W.B., Lee, S.-M., Coker, D.A., Jones, K.W., Spanne, P., 1996. Medial axis analysis of void structure in three-dimensional tomographic images of porous media. Journal of Geophysical Research: Solid Earth 101 (B4), 8297–8310.
Liu, X., Peng, C., Bai, H., Zhang, Q., Ye, G., Zhou, X., Yuan, W., 2020. A pore network model for calculating pressure drop in packed beds of arbitrary-shaped particles. AIChE J. 66 (9), e16258.
Lovreglio, P., Das, S., Buist, K.A., Peters, E.A.J.F., Pel, L., Kuipers, J.A.M., 2018. Experimental and numerical investigation of structure and hydrodynamics in packed beds of spherical particles. AIChE J. 64 (5), 1896–1907.
Mason, G., Morrow, N.R., 1991. Capillary behavior of a perfectly wetting liquid in irregular triangular tubes. J. Colloid Interface Sci. 141 (1), 262–274.
Morimoto, T., Zhao, B., Taborda, D.M.G., O'Sullivan, C., 2022. Critical appraisal of pore network models to simulate fluid flow through assemblies of spherical particles. Comput. Geotech. 150, 104900.
Øren, P.-E., Bakke, S., 2003. Reconstruction of berea sandstone and pore-scale modelling of wettability effects. J. Petrol. Sci. Eng. 39 (3–4), 177–199.
Poelma, C., 2020. Measurement in opaque flows: a review of measurement techniques for dispersed multiphase flows. Acta Mech. 231 (6), 2089–2111.
Rabbani, A., Babaei, M., 2019. Hybrid pore-network and lattice-Boltzmann permeability modelling accelerated by machine learning. Adv. Water Resour. 126, 116–128.
Raeini, A.Q., Bijeljic, B., Blunt, M.J., 2017. Generalized network modeling: Network extraction as a coarse-scale discretization of the void space of porous media. Phys. Rev. E 96 (1), 013312.
Robbins, D.J., El-Bachir, M.S., Gladden, L.F., Cant, R.S., von Harbou, E., 2012. CFD modeling of single-phase flow in a packed bed with MRI validation. AIChE J. 58 (12), 3904–3915.
Silin, D., Patzek, T., 2006. Pore space morphology analysis using maximal inscribed spheres. Physica A: Statistical mechanics and its applications 371 (2), 336–360.
Suekane, T., Yokouchi, Y., Hirai, S., 2003. Inertial flow structures in a simple-packed bed of spheres. AIChE J. 49 (1), 10–17.
Sufian, A., Knight, C., O'Sullivan, C., van Wachem, B., Dini, D., 2019. Ability of a pore network model to predict fluid flow and drag in saturated granular materials. Comput. Geotech. 110, 344–366.
I. The MathWorks, Matlab optimization toolbox - genetic algorithm, www.mathworks.com/help/gads/ga.html (version 9.6 (R2019a)).
T. Trilinos Project Website, The Trilinos Project Team, https://trilinos.github.io (version 12.18.1).
Wongkham, J., Wen, T., Lu, B., Cui, L., Xu, J., Liu, X., 2020. Particle-resolved simulation of randomly packed pebble beds with a novel fluid-solid coupling method. Fusion Eng. Des. 161, 111953.
Xiong, Q., Baychev, T.G., Jivkov, A.P., 2016. Review of pore network modelling of porous media: Experimental characterisations, network constructions and applications to reactive transport. J. Contam. Hydrol. 192, 101–117.
Yu, Z., Fan, L.S., 2010. Lattice boltzmann method for simulating particle–fluid interactions. Particuology 8 (6), 539–543.
Zeiser, T., 2002. Analysis of the flow field and pressure drop in fixed-bed reactors with the help of lattice boltzmann simulations. Philos. Trans. Roy. Soc. London Ser. A: Math., Phys. Eng. Sci. 360 (1792), 507–520.
Zeiser, T., Lammers, P., Klemm, E., Li, Y.W., Bernsdorf, J., Brenner, G., 2001. CFD-calculation of flow, dispersion and reaction in a catalyst filled tube by the lattice boltzmann method. Chem. Eng. Sci. 56 (4), 1697–1704.